Measurement of the Crab Nebula spectrum over three decades in energy with the MAGIC telescopes

J. Aleksić[a], S. Ansoldi[b], L. A. Antonelli[c], P. Antoranz[d], A. Babic[e], P. Bangale[f], J. A. Barrio[g], J. Becerra González[h,aa],
W. Bednarek[i], E. Bernardini[j], B. Biasuzzi[b], A. Biland[k], O. Blanch[a], S. Bonnefoy[g], G. Bonnoli[c], F. Borracci[f], T. Bretz[l,ab],
E. Carmona[m], A. Carosi[c], P. Colin[f], E. Colombo[h], J. L. Contreras[g], J. Cortina[a], S. Covino[c], P. Da Vela[d], F. Dazzi[f], A. De Angelis[b],
G. De Caneva[j], B. De Lotto[b], E. de Oña Wilhelmi[n], C. Delgado Mendez[m], M. Doert[o], D. Dominis Prester[e], D. Dorner[l], M. Doro[p],
S. Einecke[o], D. Eisenacher[l], D. Elsaesser[l], M. V. Fonseca[g], L. Font[q], K. Frantzen[o], C. Fruck[f], D. Galindo[r], R. J. García López[h],
M. Garczarczyk[j], D. Garrido Terrats[q], M. Gaug[q], N. Godinović[e], A. González Muñoz[a], S. R. Gozzini[j], D. Hadasch[n,ae],
Y. Hanabata[s], M. Hayashida[s], J. Herrera[h], D. Hildebrand[k], J. Hose[f], D. Hrupec[e], W. Idec[i], V. Kadenius[u], H. Kellermann[f],
K. Kodani[s], Y. Konno[s], J. Krause[f], H. Kubo[s], J. Kushida[s], A. La Barbera[c], D. Lelas[e], N. Lewandowska[l], E. Lindfors[u,ac],
S. Lombardi[c], M. López[g], R. López-Coto[a], A. López-Oramas[a], E. Lorenz[f], I. Lozano[g], M. Makariev[v], K. Mallot[j], G. Maneva[v],
N. Mankuzhiyil[b,ad], K. Mannheim[l], L. Maraschi[c], B. Marcote[r], M. Mariotti[p], M. Martínez[a], D. Mazin[f,ai], U. Menzel[f],
J. M. Miranda[d], R. Mirzoyan[f], A. Moralejo[a], P. Munar-Adrover[r], D. Nakajima[s], A. Niedzwiecki[i], K. Nilsson[u,ac], K. Nishijima[s],
K. Noda[f], N. Nowak[f], R. Orito[s], A. Overkemping[o], S. Paiano[p], M. Palatiello[b], D. Paneque[f], R. Paoletti[d], J. M. Paredes[r],
X. Paredes-Fortuny[r], M. Persic[b,af], P. G. Prada Moroni[x], E. Prandini[k], S. Preziuso[d], I. Puljak[e], R. Reinthal[u], W. Rhode[o], M. Ribó[r],
J. Rico[a], J. Rodriguez Garcia[f], S. Rügamer[l], A. Saggion[p], T. Saito[s], K. Saito[s], K. Satalecka[g], V. Scalzotto[p], V. Scapin[g],
C. Schultz[p], T. Schweizer[f], S. N. Shore[w], A. Sillanpää[u], J. Sitarek[a], I. Snidaric[e], D. Sobczynska[i], F. Spanier[l], V. Stamatescu[a,ag],
A. Stamerra[c], T. Steinbring[l], J. Storz[l], M. Strzys[f], L. Takalo[u], H. Takami[s], F. Tavecchio[c], P. Temnikov[v], T. Terzić[e], D. Tescaro[h],
M. Teshima[f], J. Thaele[o], O. Tibolla[l], D. F. Torres[x], T. Toyama[f], A. Treves[y], M. Uellenbeck[o], P. Vogler[k], R. M. Wagner[f,ah],
R. Zanin[r,ai], (The MAGIC collaboration), D. Horns[t], J. Martín[n], M. Meyer[z]

[a]IFAE, Campus UAB, E-08193 Bellaterra, Spain
[b]Università di Udine, and INFN Trieste, I-33100 Udine, Italy
[c]INAF National Institute for Astrophysics, I-00136 Rome, Italy
[d]Università di Siena, and INFN Pisa, I-53100 Siena, Italy
[e]Croatian MAGIC Consortium, Rudjer Boskovic Institute, University of Rijeka and University of Split, HR-10000 Zagreb, Croatia
[f]Max-Planck-Institut für Physik, D-80805 München, Germany
[g]Universidad Complutense, E-28040 Madrid, Spain
[h]Inst. de Astrofísica de Canarias, E-38200 La Laguna, Tenerife, Spain
[i]University of Łódź, PL-90236 Lodz, Poland
[j]Deutsches Elektronen-Synchrotron (DESY), D-15738 Zeuthen, Germany
[k]ETH Zurich, CH-8093 Zurich, Switzerland
[l]Universität Würzburg, D-97074 Würzburg, Germany
[m]Centro de Investigaciones Energéticas, Medioambientales y Tecnológicas, E-28040 Madrid, Spain
[n]Institute of Space Sciences, E-08193 Barcelona, Spain
[o]Technische Universität Dortmund, D-44221 Dortmund, Germany
[p]Università di Padova and INFN, I-35131 Padova, Italy
[q]Unitat de Física de les Radiacions, Departament de Física, and CERES-IEEC, Universitat Autònoma de Barcelona, E-08193 Bellaterra, Spain
[r]Universitat de Barcelona, ICC, IEEC-UB, E-08028 Barcelona, Spain
[s]Japanese MAGIC Consortium, Division of Physics and Astronomy, Kyoto University, Japan
[t]Institut für Experimentalphysik Univ. Hamburg, D-22761 Hamburg, Germany
[u]Finnish MAGIC Consortium, Tuorla Observatory, University of Turku and Department of Physics, University of Oulu, Finland
[v]Inst. for Nucl. Research and Nucl. Energy, BG-1784 Sofia, Bulgaria
[w]Università di Pisa, and INFN Pisa, I-56126 Pisa, Italy
[x]ICREA and Institute of Space Sciences, E-08193 Barcelona, Spain
[y]Università dell'Insubria and INFN Milano Bicocca, Como, I-22100 Como, Italy
[z]Stockholm University, Oskar Klein Centre for Cosmoparticle Physics, SE-106 91 Stockholm, Sweden
[aa]now at: NASA Goddard Space Flight Center, Greenbelt, MD 20771, USA and Department of Physics and Department of Astronomy, University of Maryland,
College Park, MD 20742, USA
[ab]now at: Ecole polytechnique fédérale de Lausanne (EPFL), Lausanne, Switzerland
[ac]now at: Finnish Centre for Astronomy with ESO (FINCA), Turku, Finland
[ad]now at: Astrophysics Science Division, Bhabha Atomic Research Centre, Mumbai 400085, India
[ae]now at: Institut für Astro- und Teilchenphysik, Leopold-Franzens-Universität Innsbruck, A-6020 Innsbruck, Austria
[af]also at INAF-Trieste
[ag]now at: School of Chemistry & Physics, University of Adelaide, Adelaide 5005, Australia
[ah]now at: Stockholm University, Oskar Klein Centre for Cosmoparticle Physics, SE-106 91 Stockholm, Sweden
[ai]Corresponding authors: R. Zanin robertazanin@gmail.com & D. Mazin mazin@mpp.mpg.de

arXiv:1406.6892v5 [astro-ph.HE] 22 Jul 2015

Abstract

The MAGIC stereoscopic system collected 69 hours of Crab Nebula data between October 2009 and April 2011. Analysis of this data sample using the latest improvements in the MAGIC stereoscopic software provided an unprecedented precision of spectral and night-by-night light curve determination at gamma rays. We derived a differential spectrum with a single instrument from 50 GeV up to almost 30 TeV with 5 bins per energy decade. At low energies, MAGIC results, combined with *Fermi*-LAT data, show a flat and broad Inverse Compton peak. The overall fit to the data between 1 GeV and 30 TeV is not well described by a log-parabola function. We find that a modified log-parabola function with an exponent of 2.5 instead of 2 provides a good description of the data ($\chi^2_{\mathrm{red}} = 35/26$). Using systematic uncertainties of the MAGIC and *Fermi*-LAT measurements we determine the position of the Inverse Compton peak to be at $(53 \pm 3_{\mathrm{stat}} + 31_{\mathrm{syst}} - 13_{\mathrm{syst}})$ GeV, which is the most precise estimation up to date and is dominated by the systematic effects. There is no hint of the integral flux variability on daily scales at energies above 300 GeV when systematic uncertainties are included in the flux measurement. We consider three state-of-the-art theoretical models to describe the overall spectral energy distribution of the Crab Nebula. The constant B-field model cannot satisfactorily reproduce the VHE spectral measurements presented in this work, having particular difficulty reproducing the broadness of the observed IC peak. Most probably this implies that the assumption of the homogeneity of the magnetic field inside the nebula is incorrect. On the other hand, the time-dependent 1D spectral model provides a good fit of the new VHE results when considering a $80 \, \mu$G magnetic field. However, it fails to match the data when including the morphology of the nebula at lower wavelengths.

Keywords: Crab Nebula, Pulsar Wind Nebulae, MAGIC telescopes, Imaging Atmospheric Cherenkov Telescopes, very high energy gamma rays

1. Introduction

The Crab pulsar wind nebula (PWN) is a leftover of the supernova explosion that occurred in 1054 A.D. (Stephenson & Green 2003), and it is powered by the pulsar PSR B0531+21 at its center (Hester 2008, for a detailed review). The Crab Nebula continuously supplies relativistic particles, mainly positrons and electrons, that advect in the magnetized wind of the neutron star. These relativistic particles are thought to be accelerated to a power-law distribution either via a Fermi-like acceleration process taking place at the termination shock (TS) (Arons & Tavani 1994, and references therein) or via shock-driven reconnection in a striped wind (Pétri & Lyubarsky 2007; Sironi & Spitkovsky 2011). The downstream flow interacts with the surrounding magnetic and photon fields creating the PWN. The nebula emits synchrotron radiation which is observed from radio frequencies up to soft γ rays. This emission is well described by the magnetohydrodynamic (MHD) model of Kennel & Coroniti (1984). At higher energies (above 1 GeV), the overall emission is instead dominated by the Inverse Compton (IC) up-scattering of synchrotron photons by the relativistic electrons in the nebula (de Jager & Harding 1992; Atoyan & Aharonian 1996).

The Crab Nebula is one of the best studied objects in the sky. Due to its brightness at all wavelengths, precise measurements are provided by different kinds of instruments, allowing for many discoveries, later seen in other non-thermal sources, and a detailed examination of its physics (Bühler & Blandford 2014, for a detailed review). The IC emission from the Crab Nebula was detected for the first time above 700 GeV by the pioneering Whipple imaging atmospheric Cherenkov telescope in 1989 (Weekes et al. 1989). Since then, the imaging Cherenkov technique has been successfully used to extend the Crab Nebula differential energy spectrum from few hundred GeV up to 80 TeV (Aharonian et al. 2004, 2006, HEGRA and H.E.S.S., respectively). However, the spectrum below 200 GeV has been observed only recently, revealing the long-anticipated IC peak in the distribution. At low energies, space-based instruments, like *Fermi*-LAT, have improved the sensitivity in the energy

range between few and hundred GeV (Abdo et al. 2010); whereas, on the other side, ground-based imaging atmospheric Cherenkov telescopes (IACTs) with larger reflective surface reached lower energy thresholds, below 100 GeV. The observations carried out by the stand-alone first MAGIC[1] telescope (MAGIC-I) showed a hardening of the spectrum below a few hundred GeV (Albert et al. 2008a). However, in previous studies using MAGIC-I and *Fermi*-LAT measurements, the spectral overlap required to make a precision measurement of the IC peak energy was not achieved. Moreover, the quality of the available data around the IC peak was insufficient to rule out existing PWN models or at least distinguish between them. The goal of this work is to use the MAGIC stereoscopic system to measure, with high statistical precision, the Crab Nebula differential energy spectrum down to energies of 50 GeV, and to compare this spectral measurement with state-of-the-art PWN models.

The Crab Nebula was adopted as a standard candle in many energy regimes, due to its high luminosity and apparent overall long-term flux stability. It has been used to cross-calibrate X-ray and γ-ray telescopes, to check the instrument performance over time, and to provide units for the emission of other astrophysical objects. However, in 2010 September, both *AGILE* and *Fermi*-LAT detected an enhancement of the γ-ray flux above 100 MeV (Tavani et al. 2011; Abdo et al. 2011). Variability has also been measured in X rays on yearly time scale (Wilson-Hodge et al. 2011). A search for possible flux variations in MAGIC data coinciding with the GeV flares will be discussed in a separate paper.

2. Observations and analysis

MAGIC currently consists of two 17 m diameter IACTs located in the Canary Island of La Palma (Spain) at a height of 2200 m above sea level. It is sensitive to very-high-energy (VHE) γ rays in the energy range between a few tens of GeV and a few tens of TeV. MAGIC started operations in autumn 2004 as a single telescope, MAGIC-I, and became a stereoscopic system five years later in 2009. During the summers 2011 and 2012, MAGIC underwent a major upgrade involving the readout systems of both telescopes and the MAGIC-I camera (Aleksić et al. 2014a). The stereoscopic observation mode led to a significant improvement in the performance of the instrument with an increase in sensitivity by a factor of more than two, while the upgrade, meant to equalize the performance of the two telescopes, improved the sensitivity of the instrument mainly at energies below 200 GeV (Aleksić et al. 2014b).

In this work we use MAGIC stereoscopic observations of the Crab Nebula carried out between October 2009 and April 2011, before the above-mentioned upgrade[2]. The instrument performance in this period, described in detail in Aleksić et al. (2012), was sufficient to measure a point-like source with a power-law photon index of 2.6 and an integral flux of 9×10^{-13} cm^{-2} s^{-1} above 300 GeV, at 5-σ in 50 h of low zenith angle observations. The selected data set includes observations performed in *wobble* mode (Fomin et al. 1994) at zenith angles between 5° and 62°. Data affected by hardware problems, bad atmospheric conditions, or displaying unusual background rates were rejected to ensure a stable performance, resulting in 69 h of effective time.

The analysis was performed by using the tools of the standard MAGIC analysis software (Zanin et al. 2013). Each telescope records only the events selected by the hardware stereo trigger. For every event the image cleaning procedure selects the pixels which have significant signal and removes the rest. The obtained reconstructed image is then quantified with a few parameters. For the analysis of the Crab Nebula data set we used *sum image cleaning*, a new algorithm which lowers the analysis energy threshold to 55 GeV and provides a 15% improvement in sensitivity below 150 GeV (Lombardi 2011).

After the image cleaning procedure, stereoscopic pairs of images are combined and the shower direction is determined as the crossing point of the corresponding single-telescope di-

---

[1] Major Atmospheric Gamma Imaging Cherenkov

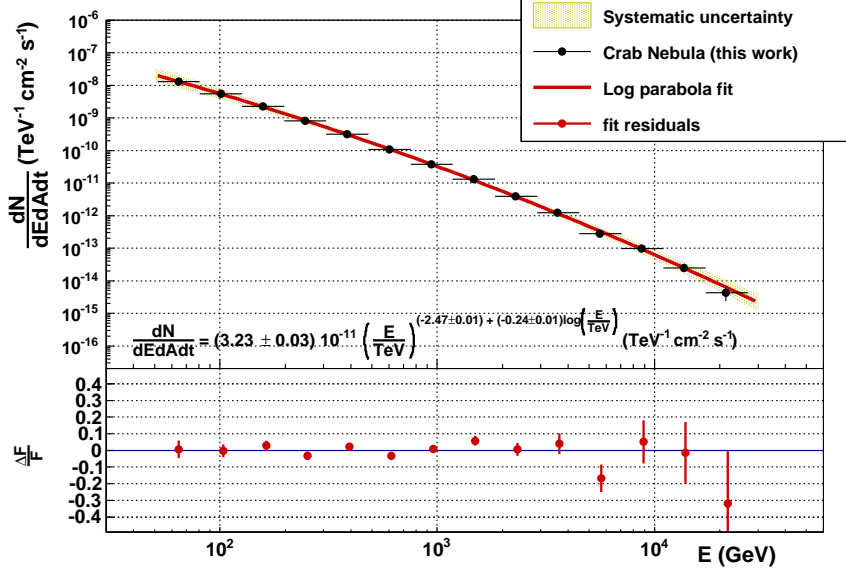[2] Data after the upgrade are currently being studied and will be matter of a forthcoming publication.

Figure 1: Differential energy spectrum of the Crab Nebula obtained with data recorded by the MAGIC stereoscopic system.

rections. The reconstruction of the shower direction is later improved by applying an upgraded version of the *disp* method (Zanin et al. 2013). The background rejection relies on the definition of the multi-variable parameter *hadronness*, which is computed by means of a Random Forest (RF) algorithm (Albert et al 2008b). RF uses as input a small set of image parameters from both telescopes, together with the information about the height of the shower maximum in the atmosphere provided by the stereoscopic reconstruction. The γ-ray signal is estimated through the distribution of the squared angular distance (θ^2) between the reconstructed and the catalog source position. The energy of each event is estimated by using look-up tables created from Monte Carlo (MC) simulated γ-ray events. For the computation of the differential energy spectrum, the γ-ray signal in each energy bin is determined by selecting a soft *hadronness* cut, which retains 90% of the γ-ray events ensuring a good agreement between data and MC. Next, an unfolding procedure is applied to the obtained differential energy spectra to correct for the energy bias and the finite energy resolution of the detector. In particular, we apply five different unfolding methods described in Albert et al. (2007) and check the consistency of the results. For the light curves, we compute integral γ-ray fluxes in a given energy range as a function of time. No full-fledged unfolding

procedure is used here. Instead, a correction is applied to the effective area in the selected energy range to account for the spillover of the Monte Carlo simulated events with (true) energy outside of it, under the assumption of a given shape of the differential energy spectrum.

Since our data set spans a large zenith angle range (5° to 62°), we divide the data sample in three zenith angle ranges[3] to better account for corresponding variations in the image parameters: a) 5° to 35°, b) 35° to 50°, and c) 50° to 62°. The matrices for the background rejection obtained through the RF, as well as the look-up tables for the energy estimation, are computed separately for each sub-sample. The three independent analyses are then combined with the spectral unfolding procedure.

3. Results

3.1. The differential energy spectrum

The main result of this work, shown in Figure 1, is the differential energy spectrum of the Crab Nebula obtained with a single instrument covering almost three decades in energy, from 50 GeV up to 30 TeV, and spanning seven orders of magnitude in flux. It is unfolded with Tikhonov's method (Tikhonov & Arsenin

---

[3]The binning in zenith angle (zd) is equidistant in cos(zd).

1979), but all the other considered unfolding methods provide compatible results within the statistical errors. The spectrum has five spectral points per energy decade and statistical errors as low as 5% below 150 GeV. Below 10 TeV, the overall uncertainty is dominated by systematic, rather than statistical, uncertainties. The systematic uncertainties, displayed in Figure 1 as the shaded area, will be discussed in detail below.

The overall IC emission from the Crab Nebula, as well as many other PWNe, is usually approximately described by a log-parabola function ($dN/dE = f_0 \left(\frac{E}{E_0}\right)^{-\alpha+\beta \log(E/E_0)}$). However, other functional forms can provide good fits of the measured VHE emission from the Crab Nebula over specific energy sub-ranges. In literature, between ~0.5 and 50–80 TeV, the Crab Nebula spectrum was described by either a power law (Aharonian et al. 2004, $dN/dE = f_0 \left(\frac{E}{E_0}\right)^{-\alpha}$) or a power law with an exponential cut off (Aharonian et al. 2006, $dN/dE = f_0 \left(\frac{E}{E_0}\right)^{-\alpha} \exp\left(-\frac{E}{E_c}\right)$). We considered both a log-parabola and a power law with an exponential cut off for the analytical description of the new spectral energy points presented in this work. The single power-law function fails in representing them over the wide energy range covered by the new MAGIC measurement due to an obvious curvature in the measured spectrum.

The fits do not include systematic uncertainties, but they take into account the correlations between the spectral energy points. The power law with exponential cut off (not shown in the figure) results in a flux normalization $f_0 = (3.80 \pm 0.11)$ 10^{-11} TeV^{-1} cm^{-2} s^{-1}, a photon index $\alpha = 2.21 \pm 0.02$, and a cut off at $E_c = (6.0 \pm 0.6)$ TeV with a $\chi^2_{\rm red}$ of 35/11. The low fit probability is mainly due to the disagreement between the sharp cut off predicted by the fit function and the MAGIC data. As a result the three highest flux points lie above the fit function. Excluding them and repeating the fit we obtain a good fit quality of $\chi^2_{\rm red} = 8/8$. The fit to the log-parabola gives a flux normalization $f_0 = (3.23 \pm 0.03)$ 10^{-11} TeV^{-1} cm^{-2} s^{-1}, a photon index $\alpha = 2.47 \pm 0.01$, and a curvature parameter $\beta = -0.24 \pm 0.01$. It has a $\chi^2_{\rm red}$ of 20/11. The energy E_0 was fixed at 1 TeV for both fits. The log-parabola provides a better fit compared to the

power law with exponential cut off. In the bottom panel of Figure 1, one can see residuals between our measurements and the best fit. The fit results for the power law with exponential cut off and log-parabola are summarized in Table 1.

Parameter	Power law with cutoff	Log-parabola
f_0 (TeV^{-1} cm^{-2} s^{-1})	(3.80 ± 0.11) 10^{-11}	(3.23 ± 0.03) 10^{-11}
index α	2.21 ± 0.02	2.47 ± 0.01
curvature β	—	-0.24 ± 0.01
cutoff E_c (TeV)	6.0 ± 0.6	—
$\chi^2_{\rm red}$	35/11	20/11

Table 1: Best-fit parameters to the differential photon spectrum of the Crab Nebula obtained with MAGIC in the energy range between 50 GeV and 30 TeV.

The overall systematic uncertainty affecting the measurement of the differential energy spectrum of the Crab Nebula includes three different classes of effects: one on the energy scale, the second in the flux normalization and the third on the spectral shape. We considered all the sources of systematic uncertainty stated in Table 4 in Aleksić et al. (2012), and, in addition, the effect of the different zenith angle observations. The uncertainty on the energy scale is 15–17%, and for the flux normalization is about 11% (Aleksić et al. 2012). The estimation of the systematic error on the spectral shape is unique to this work since we further split the error into an uncertainty on the photon index and one on the curvature parameter, given the assumed log-parabola spectral shape. Both include a common uncertainty of 0.04 due to the non-linearity of the analog signal chain (Aleksić et al. 2012) and an individual uncertainty due to the analysis methods. The latter is evaluated as the RMS of the distributions of the α and the β parameters derived from different analyses performed with various RFs, different image cleaning algorithms, observation zenith angles, and efficiency of γ-ray selection cuts. This yields a systematic uncertainty on α of 0.03 and on β of 0.05. The overall systematic uncertainty for both α and β is calculated by summing up in quadratures these values to the above-mentioned uncertainty of 0.04 for the effect of the non-linearity, obtaining an overall of 0.05 and 0.07 for α and β, respectively.
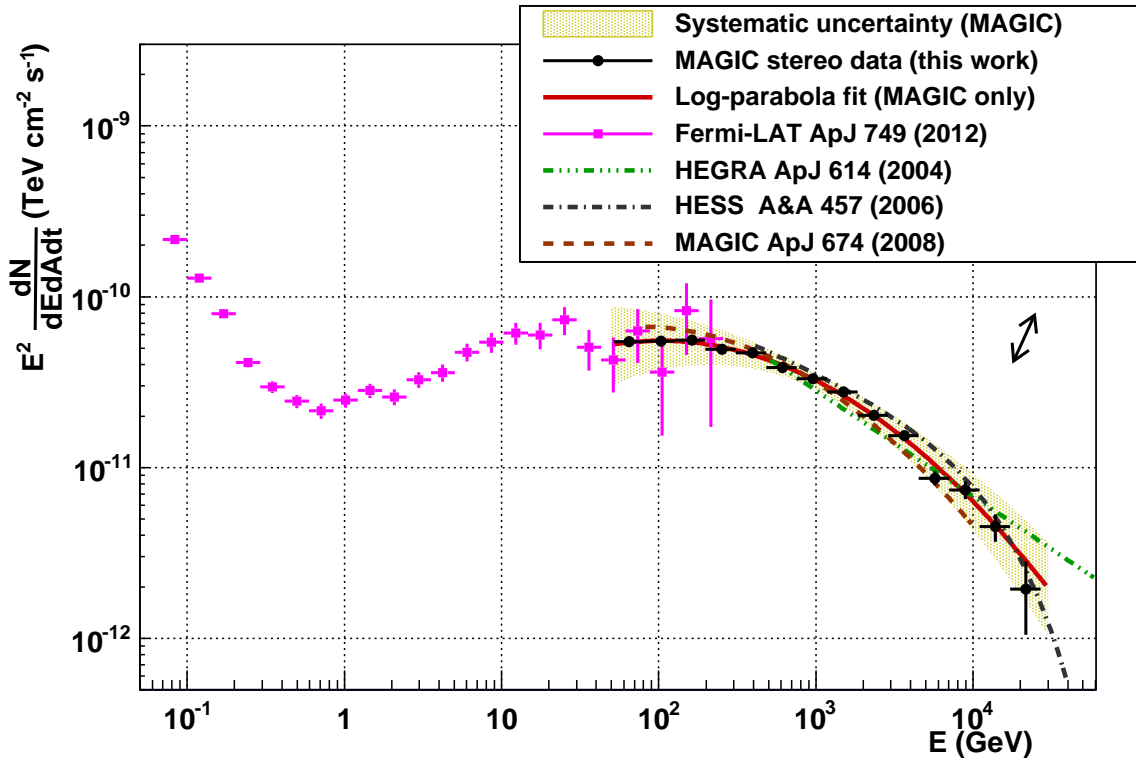
Figure 2: Spectral energy distribution of the Crab Nebula from 100 MeV to ~30 TeV obtained by *Fermi*-LAT and MAGIC, together with the fit results from other γ-ray experiments. The black arrow indicates the systematic uncertainty on the energy scale, whereas the shaded area indicates the systematic uncertainty on the flux normalization and the photon index. The solid red line is the log-parabola fit to the MAGIC data alone (the same as in Fig.1).

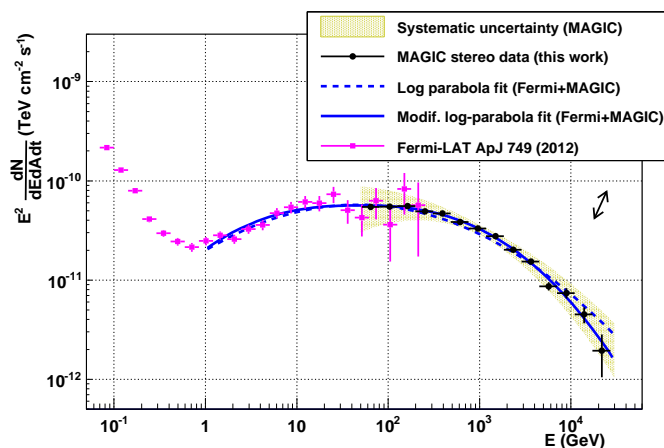## 3.2. *Spectral energy distribution of the Crab Nebula*

Figure 3: Spectral energy distribution of the Crab Nebula obtained by *Fermi*-LAT and MAGIC. The two lines indicate the results of the fits to the combination of *Fermi*-LAT and MAGIC spectral points, see text for details.

Figure 2 shows the spectral energy distribution (SED) for the MAGIC data (same data set as used for Figure 1), and compares it to the measurements by other IACTs (green, black and brown lines) as well as to the *Fermi*-LAT results for the Crab Nebula (magenta squares). In this work we used the latest *Fermi*-LAT published results on the Crab Nebula, which include 33 months of data (Buehler et al. 2012). At low energies (50–200 GeV), MAGIC data overlaps with the *Fermi*-LAT measurements, showing an agreement, within the statistical errors, between the spectral points of the two instruments. At higher energies (above 10 TeV), a disagreement between HEGRA (Aharonian et 2004) and H.E.S.S. (Aharonian et al. 2006) measurements has been noted (green dash-triple-dotted and black dash-dotted lines, respectively). This may be due to systematic uncertainties between the two instruments or may indicate a real spectral variability of the nebula. The relatively large systematic uncertainty of the MAGIC measurement and the lack of MAGIC data above 30 TeV do not support either hypothesis. Since the new MAGIC spectrum is statistically limited at these energies, we may improve the result in the future by taking a significant amount of
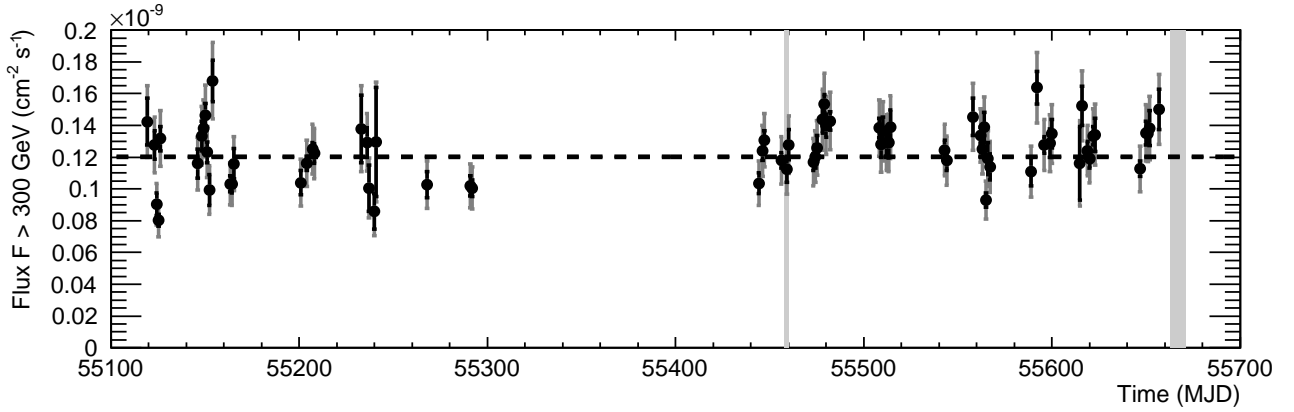
Figure 4: Daily light curve of the Crab Nebula for energies above 300 GeV. The black vertical lines show statistical error bars, the grey ones the quadratic sum of statistical errors and a 12% systematic point-wise uncertainty. The dashed horizontal line is the best fit value to a constant flux. The grey areas indicate the Crab flares as reported by AGILE and *Fermi*-LAT.

additional Crab Nebula data with MAGIC.

To ensure independence from theoretical modeling, and assuming that the easiest approximation for the IC contribution of the Crab Nebula emission is a log-parabolic shape, we estimate the position of the IC peak by a log-parabola fit to the data. In all fits described below we take the correlations between MAGIC spectral points into account and consider only statistical errors unless stated otherwise. The fit to the MAGIC data alone can locate the IC peak and doing so results in (103 ± 8) GeV ($\chi^2_{\mathrm{red}} = 20/11$), consistent with the earlier single telescope MAGIC result ((77 ± 47) GeV, Albert et al. 2008a). A more robust fit result is obtained by considering of MAGIC and *Fermi*-LAT spectral data together since they cover both sides of the IC peak. We, therefore, perform a joint fit to the MAGIC and *Fermi*-LAT spectral data points starting from 1 GeV, corresponding to the energy of the lowest spectral point of the *Fermi*-LAT spectrum where the IC contribution dominates over synchrotron emission. The best fit result ($\chi^2_{\mathrm{red}} = 82/27$) is shown as dashed line in Figure 3. It results in an IC peak position at (53 ± 3) GeV.

In the following we investigate how systematic uncertainties of the instruments may alter the fit result. First, we include an ad-hoc point-wise flux uncertainty to MAGIC data. We would need an additional point-wise flux uncertainty of $>$ 25% in order to obtain an acceptable fit with a probability larger than 5%. Such ad-hoc uncertainty exceeds both MAGIC and

Fermi-LAT systematic errors on the flux normalization. Second, we allow a shift in the energy scale of the MAGIC data relative to the *Fermi*-LAT data[4], the best fit ($\chi^2_{\mathrm{red}} = 74/26$) locates the IC peak at (69 ± 7) GeV, for a +11% shift. Third, we consider bracketing cases in the MAGIC systematic uncertainty in the energy scale (15%), in the MAGIC flux normalization (11%), in the *Fermi*-LAT flux normalization (5%), and in the *Fermi*-LAT energy scale (+2% and -5%). The resulting IC peak positions using any combination of the considered uncertainties range from 40 GeV up to 84 GeV. Thus, we determine the IC peak position to $(53\pm3_{\mathrm{stat}}+31_{\mathrm{syst}}-13_{\mathrm{syst}})$ GeV including the systematic uncertainties of the two instruments and assuming that the peak can be described by a log-parabola. However, none of the combinations (fits performed) resulted in an acceptable fit quality. The highest fit probability obtained is 10^{-5}. We, therefore, conclude that the quality of the data presented here shows clearly that the log-parabola cannot be used to describe the IC peak over an energy range spanning four decades even considering systematic uncertainties of MAGIC and *Fermi*-LAT.

To further conclude on the actual IC peak position we investigated different fit ranges and also looked for a spectral model which better reproduces the new observational results. We find

---

[4]We consider *Fermi*-LAT to be better calibrated since it was absolutely calibrated with test beams at CERN before launch (Atwood et al. 2009), whereas there is no test beam for the IACT technique.

that the log-parabola is a good fit ($\chi^2_{\mathrm{red}} = 14/13$) if considering data in a small region around the peak only, namely between 5 GeV and 500 GeV: The IC peak is then at (51 ± 11) GeV. To improve the likelihood of the fit in the whole IC component regime (1 GeV – 30 TeV), we considered functions with extra free parameters. The most satisfactory fit is achieved using a modified log-parabola function:

$E^2 \times dN/dE = 10^{\log f_0 + C\left(\log\left(\frac{E}{E_{IC}}\right)\right)^a}$. Such a fit function, with one more free parameter a than a log-parabola discussed above, provides acceptable results with a $\chi^2_{\mathrm{red}} = 35/26$, locating the IC peak at $E_{IC} = (48 \pm 2)$ GeV. The resulting exponent $a = 2.5 \pm 0.1$ produces a flatter peak than the one obtained by the canonical quadratic function, see both fit functions in Fig. 3. The other fit parameters are: $C = -10.248 \pm 0.006$ and $\log(f_0) = -0.120 \pm 0.008$, both in units of $[log(\mathrm{TeV/cm2/s})]$. Also a power law function with a sub-exponential cutoff

$E^2 \times dN/dE = N_0 \left(\frac{E}{E_0}\right)^{-\alpha} \exp\left(-E/E_{\mathrm{cutoff}}\right)^\beta$ provides an acceptable fit ($\chi^2_{\mathrm{red}} = 39/26$) with $N_0 = (6.8 \pm 0.6)$ TeVcm^{-2}s^{-1}, $\alpha = 1.59 \pm 0.02$, $E_{\mathrm{cutoff}} = (20.8 \pm 3.9)$ GeV and $\beta = 0.285 \pm 0.006$. The maximum in such mathematical approximation is reached at 76 GeV.

Even though the fit functions above provide a good fit to the joint data set without any shift in energy scale or flux normalization, they are not physically motivated. We note that the fit functions and fit ranges we exploited here yield a peak position within the systematic uncertainties of the log-parabola fit stated above.

3.3. The light curve

In this section we present the light curve above 300 GeV from the Crab Nebula. This is meant to check the flux stability on time scales of days. The results are presented in Figure 4, which shows the MAGIC daily fluxes between October 15, 2009 and April 6, 2011, where the error bars indicate statistical (shown in black) and systematic errors (the combined error is shown in grey). The average flux above 300 GeV F$_{>300\mathrm{GeV}}$ is:

$$\mathrm{F}_{>300\mathrm{GeV}} = (1.20 \pm 0.08_{stat} \pm 0.17_{sys}) \times 10^{-10} \mathrm{cm}^{-2}\mathrm{s}^{-1}$$

The systematic error on the integral flux is estimated to be 14%, excluding any possible shift in the energy scale. The derived Crab Nebula flux is stable (fit by a constant has a probability of 15%) within statistical errors and a 12% systematic point-wise uncertainty, added in quadrature. This agrees with the systematic uncertainty expected for run-to-run data obtained in Aleksić et al. (2012). Note that the systematic uncertainty in Aleksić et al. (2012) was computed using the same source, the Crab Nebula. Thus, we cannot completely exclude the intrinsic variability at a level below 12%. This point-wise systematic uncertainty is attributed mainly to the transmission of the atmosphere for the Cherenkov light, which can change on a daily basis or even faster due to variations in the weather conditions, and the mirror reflectivity, which can change due to the deposition of dust. The grey areas correspond to the Crab flares at energies above 100 MeV as reported by AGILE and *Fermi*-LAT. MAGIC observed the Crab Nebula simultaneously during the flare that occurred on MJD = 55458 – 55460[5] but no enhanced activity above 300 GeV was detected.

4. Discussion

There are two broad classes of PWN models which have been used to describe the observed broad band synchrotron and IC emission of PWNe: models which consider the MHD solution of the downstream flow (Kennel & Coroniti 1984; de Jager & Harding 1992; Atoyan & Aharonian 1996; de Jager et al. 1996; Del Zanna et al. 2006; Volpi et al. 2008; Meyer et al. 2010), and models with a simplified one-zone approach either with a constant and isotropic magnetic field in a static setting (Hillas et al. 1998; Aharonian et al. 2004; Meyer et al. 2010) or tracing the PWN evolution (Bednarek & Bartosik 2003, 2005; Martín et al. 2012).

The broad-band SED of the Crab Nebula has been tested against models in the two categories:

- an MHD flow model assuming a spherical symmetry as in Kennel & Coroniti (1984) and presented in Meyer et al. (2010).

---

[5]The MAGIC data are centered around MJD = 55459.2

- a model based on the one first suggested by Hillas et al. (1998) assuming a static, constant magnetic field, *B* and described in Meyer et al. (2010).

- a time-dependent spherically symmetric (1D) PWN spectral model presented in Martín et al. (2012).

4.1. MHD flow model

The MHD flow model is based on the analytical modelization of the structure of the downstream pulsar wind for the simplified case of a spherical symmetric ideal MHD flow, as in Kennel & Coroniti (1984). The solution of the MHD flow depends on the magnetization parameter σ, the (known) spin-down power of the pulsar, and the position of the TS r_{TS}. The injection spectrum of the particles is parameterized to be a power-law with a cutoff and is left free to fit the observed emission spectrum. The observed emission spectrum is calculated by self-consistently calculating the synchrotron emissivity of the electron distribution which is carried by the flow taking into account synchrotron and adiabatic cooling losses. The resulting photon density is used to calculate the IC emissivity. Also the emission of the dust is considered as additional photon field, as described in Meyer et al. (2010). The resulting spectrum is compared with the measurements and the free parameters are minimized using a χ^2 cost function. For an assumed value of $\sigma = 0.0045$ (Meyer et al. 2010), $r_w = 0.14$ pc, and $L_{sd} = 5 \times 10^{38}$ ergs/s the minimum value of χ^2_{red}=2.3/254, including a relative systematic uncertainty of 7 %. While the fit is reasonably good for the synchrotron part of the spectrum, the IC part adds a $\Delta\chi^2 \approx 200$ to the fit, indicating that the spatial structure of the magnetic field is not consistent with the data.

4.2. Static, constant B-field model

The *constant B-field model* was introduced in Meyer et al. (2010) and follows the prescription put forward in Hillas et al. (1998) and Aharonian et al. (2004). The Crab Nebula is assumed to be homogeneously filled with a constant magnetic field and two distinct electron populations: relic electrons (responsible for the radio synchrotron emission) and wind electrons. The relic electron population is needed to explain the

break in the synchrotron spectrum at optical wavelengths (see also Section 6 in Meyer et al. 2010). The relic electrons might be the result of a rapid spin-down phase in the early stages of the evolution of the Crab Nebula (Atoyan 1999). The populations can be regarded as averaged representations of the electron distributions. The two spectra were modeled with a simple power law and a broken power law with a super-exponential cut off for relic and wind electrons, respectively. For their definition we refer the reader to Meyer et al. (Eqs. (1) and (2) in 2010). The minimal gamma factor of the relic electrons was fixed to 3.1 in the fit as it is not constrained by the observable part of the SED. Following Hillas et al. (1998), the spatial distributions of both the seed photons and pulsar wind electrons were described with Gaussian functions in distance to the nebula's center (see discussion and Eqs. (A.1) and (A.2) in Meyer et al. 2010), whereas the relic electron population is uniformly distributed throughout the nebula. The variances of the Gaussian distributions vary with energy, thus accounting for the observed smaller size of the nebula at shorter wavelengths. The thermal dust emission was assumed to follow a gray body spectrum. Its extension was fixed in the fit ($\theta_{\mathrm{dust}} = 1.3'$ following Hillas et al. 1998), while, in contrast to Meyer et al. (2010), the values of remaining dust parameters were allowed to float.

The electron spectra were calculated using the same synchrotron data as in Meyer et al. (2010) except for the new *Fermi*-LAT data (Buehler et al. 2012). For a given magnetic field strength, the parameters of the electron spectra were derived from the fit to the synchrotron data between $4 \cdot 10^{-6}$ eV $\leqslant \nu \leqslant 0.4$ GeV, using a χ^2 minimization implemented with the interface of MINUIT (James 1998). Subsequently, the magnetic field and the parameters describing the thermal dust emission were varied until the IC part of the SED (E > 0.4 GeV) presented in this work is reproduced best. The full Klein-Nishina cross section is used to calculate the IC emission including synchrotron and thermal dust emission, and the cosmic microwave background (CMB).

Allowing for a point-wise systematic uncertainty of 8% of the flux (added in quadrature, Meyer et al. 2010), the synchrotron emission is accurately reproduced with $\chi^2_{\mathrm{red}} = 249/217 = 1.15$
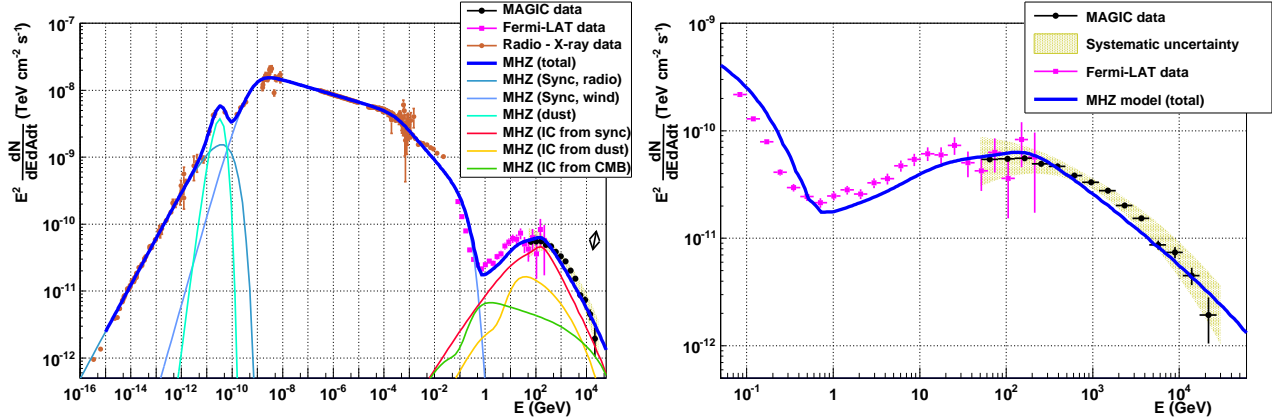
Figure 5: *On the left:* The overall spectral energy distribution of the Crab Nebula from radio to γ rays. Lines are best fit results based on the model of Meyer et al. (2010) (MHZ), see text for details. The thin lines show individual components of the photon spectrum (see the inlay), and the thick blue line identifies the overall emission. Historical data (brown) are from Meyer et al. (2010), *Fermi*-LAT data (pink) are from Buehler et al. (2012), and the VHE data are from this work. *On the right:* Zoom in the γ-ray regime.

Table 2: Best-fit parameters for the constant *B*-field model. The definition of the model parameters is given in Meyer et al. (2010).

Magnitude	Crab Nebula
Magnetic field	
$B\,(\mu G)$	143
Dust component	
$\ln(N_{\mathrm{dust}})$	-29.9
T_{dust} (K)	98
$u_{\mathrm{dust}}(\mathrm{eV\,cm^{-3}})$	1.2
Radio electrons	
S_r	1.6
$\ln N_r$	119.8
$\ln \gamma_r^{\mathrm{min}}$	3.1
$\ln \gamma_r^{\mathrm{max}}$	12
Wind electrons	
S_w	3.2
ΔS	0.6
$\ln N_w$	78.5
$\ln \gamma_w^{\mathrm{min}}$	12.9
$1/\ln \gamma_w^{\mathrm{break}}$	-19.5
$\ln \gamma_w^{\mathrm{max}}$	22.7
β	4

(Figure 5). Above 0.4 GeV, the data is poorly described and the fit only converges if an ad-hoc (unrealistically large) systematic uncertainty of 17 % is assumed, resulting in $\chi^2_{\mathrm{red}} = 48.8/31 = 1.57$.

The final best-fit parameters are given in Table 2. Due to the small fit probability and the dependence of the fit errors on the additional ad-hoc systematic uncertainty added to the flux points, we neglect these uncertainties. When comparing the result of Meyer et al. (2010) with the one presented here, $B = 143\,\mu G$, we note that a higher value of the B-field is preferred compared to the 2010 paper in order to reproduce the MAGIC data around the IC peak. The higher quality (i.e. smaller error bars) of the *Fermi*-LAT data together with the MAGIC data shows a rather flat peak now, which cannot be reproduced in the model. If we would repeat the exact procedure from the 2010 paper and only use the updated *Fermi*-LAT data, we would find a lower B-field and the model would undershoot the MAGIC data at almost all energies. We, therefore, conclude that the constant *B*-field model cannot reproduce the flat peak of the IC SED. For energies above the peak, the predicted spectrum is too soft with too little curvature as compared to the new MAGIC data.
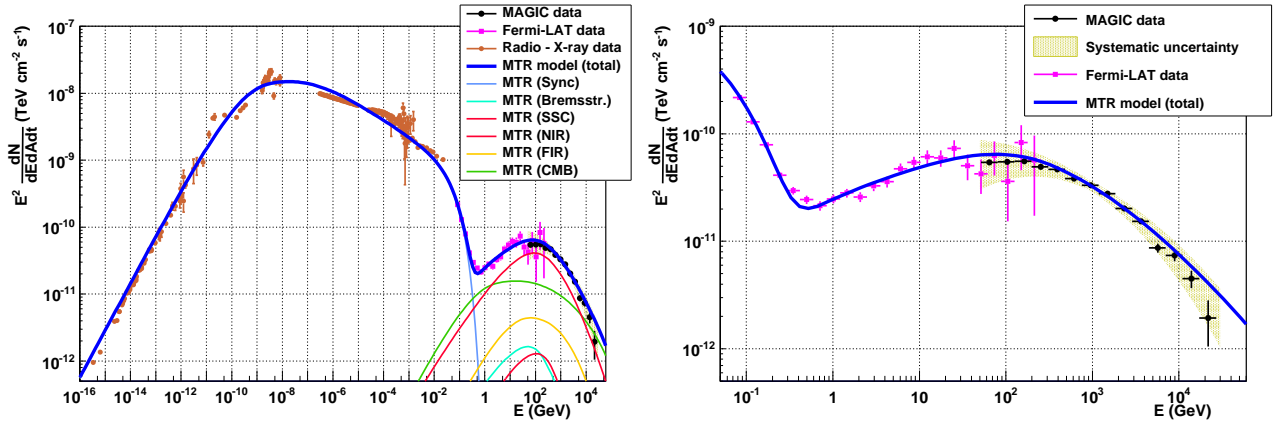
10

Figure 6: *On the left:* The overall spectral energy distribution of the Crab Nebula from radio to γ rays. Lines are best fit results based on Martín et al. (2012) (MTR), see text for details. The thin lines show individual components of the photon spectrum (see the inlay), and the thick blue line identifies the overall emission. Historical data (brown) are from Meyer et al. (2010), *Fermi*-LAT data (pink) are from Buehler et al. (2012), and the VHE data are from this work. *On the right:* Zoom in the γ-ray regime.

4.3. Time-dependent model

The time-dependent, leptonic spectral model for an isolated PWN (Martín et al. 2012; Torres et al. 2013a,b) was also considered. Such model solves the diffusion-loss equation numerically devoid of any approximation, considering synchrotron, IC and Bremsstrahlung energy losses. For the IC losses, the Klein-Nishina cross section is used. Escaping particles due to Bohm diffusion are also taken into account. The injection spectrum of the wind electrons is a broken power law normalized using the spin-down power of the pulsar and the magnetic fraction[6]. The 1D uniform magnetic field is evolved by solving the magnetic field energy conservation, including its work on the environment (Torres et al. 2013b). Considering the young age of the remnant, the nebula was treated as freely expanding. The magnetic fraction of the nebula (η) was assumed constant along the evolution, and it was used to define the time-dependent magnetic field. The model here is essentially the same as the one shown in Torres et al. (2013a) except for the incorporation of a more precise dynamical evolution to fix the nebula radius taking into account the variation of the spin-down power in time. In particular, the evolution of the radius of the nebula was calculated solving numerically Eq. (25) in van der Swaluw et al.

(2001). All other time dependent parameters were left free to evolve with the PWN. The resulting electron population was used to compute the synchrotron, IC from CMB, far infrared (FIR), and near infrared (NIR) photon fields, as well as the synchrotron self-Compton (SSC) and bremsstrahlung spectra.

The results obtained by our qualitative fit are shown in Figure 6, whereas the parameter values are listed in Table 3. The free parameters of the fit relate to the definition of the environment, of the wind electron spectrum, and the magnetization. For the former, they are essentially those describing the target photon fields with which the electrons in the nebula interact. The parameters of the wind spectrum are those contained in the broken power law assumed to describe the electrons. The other parameters are fixed or strongly constrained. Since the fit is qualitative (we are aware that by having many simplifications the model can only be considered as qualitative description of the nebula), we do not provide uncertainties on the fit parameters. We find that a low magnetic fraction of the nebula (of only a few percent) with a magnetic field of approx. $80\,\mu$G provides a good fit to the nebula measurements at the current age. Such magnetic field strength is also motivated from morphological MHD studies (Volpi et al. 2008).

We note some caveats regarding this model. It includes no structural information: the size of the synchrotron sphere is

---

[6]The magnetic fraction is the percentage of the spin down that goes into the magnetic field.

11

Table 3: Fit parameters for the time-dependent model obtained with the new data points given by *MAGIC*. The definition of the parameters can be found in Martín et al. (2012).

Magnitude	Crab Nebula
Pulsar magnitudes	
P (ms)	33.40
$\dot{P}$ (s s^{-1})	4.21×10^{-13}
τ_c (yr)	1260
t_{age} (yr)	960
$L(t_{age})$ (erg s^{-1})	4.3×10^{38}
L_0 (erg s^{-1})	3.0×10^{39}
n	2.509
τ_0 (yr)	730
d (kpc)	2
M_{ej} (M$_\odot$)	8.5
R_{PWN} (pc)	2.2
Magnetic field	
$B(t_{age})(\mu G)$	80
η	0.025
Wind electrons	
$\gamma_{max}(t_{age})$	8.3×10^9
γ_b	1×10^6
α_l	1.6
α_h	2.5
ϵ	0.25
R_{syn}/R_{PWN}	1
Target photon fields and environment density	
T_{FIR} (K)	70
w_{FIR} (eV cm^{-3})	0.1
T_{NIR} (K)	5000
w_{NIR} (eV cm^{-3})	0.3
n_H (cm^{-3})	1
T_{CMB} (K)	2.73
w_{CMB} (eV cm^{-3})	0.25

taken as the size of the nebula itself, at all frequencies as in, e.g., Bucciantini et al. (2011) or in Tanaka & Takahara (2010). This is not the case for Crab though: the size of the nebula decreases towards the optical frequencies, being always smaller than the one obtained from the use of a dynamical free expansion solution. For instance, Hillas et al. (1998) use a radius of approximately 0.4 pc up to 0.02 eV, and slightly smaller for larger energies. If this energy-dependent size of the synchrotron nebula is adopted (one-zone spheres of different sizes at different frequencies), the SSC emission would be overproduced. A full description of such a rich data set requires a more detailed model that, in addition to being time dependent, treats the morphology at different frequencies using a multi-zone, multi-dimensional approach.

5. Conclusions

We presented a long term data set of the Crab Nebula taken with the MAGIC telescopes between October 2009 and April 2011. We derived the differential energy spectrum of the Crab Nebula with one single instrument, covering almost three decades in energy, from 50 GeV up to 30 TeV. The energy spectrum in this range is clearly curved and matches well both with the *Fermi*-LAT spectrum at lower energies and with the previous Crab Nebula measurements by Whipple, HEGRA, H.E.S.S. and early MAGIC-I data. The resulting IC peak is broad and rather flat in the energy range from 10 GeV to 200 GeV. When considering the joint MAGIC–*Fermi*-LAT fit, the function which best describes this emission component is a modified log-parabola (with a 2.5 exponent). Thanks to the large lever arm of the fit we determined the most precise IC peak position at energy $((53 \pm 3_{stat} + 31_{syst} - 13_{syst}))$ GeV. The MAGIC spectrum extends up to 30 TeV but we cannot distinguish between a power law tail extending up to 80 TeV (HEGRA, Aharonian et al. 2004) and a spectral cutoff at around 14 TeV (H.E.S.S., Aharonian et al. 2006). Irrespective off spectral variability or any other sources for this discrepancy, the uncertainties do not permit a resolution of this issue. We also show that the light curve of the Crab Nebula above 300 GeV is stable within the statistical and sys-

tematic uncertainties on the daily basis (~ 12%) during the considered period. Flux stability on longer time scales, as well as data taken simultaneously with the Crab flares will be discussed elsewhere.

The statistical precision of the MAGIC data set, spanning for the first time from 50 GeV to 30 TeV, allows for a detailed test of the two state-of-the-art Crab Nebula models. The conclusion, based on earlier data, that simple models can account for the observed spectral shape has to be revisited in the light of the new MAGIC results. The MHD flow model (Meyer et al. 2010) assuming a spherically symmetry fails to reproduce the IC observations, suggesting that such a simplified structure of the magnetic field is not realistic. The constant B-field model (Meyer et al. 2010) leads to a rather poor fit to the new VHE measurements, failing to reproduce the breadth of the observed IC peak. Most probably this implies that the assumption of the homogeneity of the magnetic field inside the nebula is incorrect. The time dependent 1D model by Martín et al. (2012) can satisfactorily reproduce the VHE data up to few TeV under the assumptions of a low magnetic field of less than hundred μG. It fails, however, to provide a good fit of the new spectral data if the observed morphology of the nebula (smaller size at shorter wavelengths, as in Hillas et al. 1998) is adopted. Therefore, we conclude that more theoretical work on the Crab Nebula modeling must be done to simultaneously fit the observed morphology and the spectral energy distribution. The broad-band IC spectrum is in principle sensitive to the spatial structure of the magnetic field and hence can be used for future models.

Acknowledgements

References

Abdo, A. A., Ackermann, M., Ajello, M., et al. 2011, Science, 331, 739

—. 2010, The Astrophysical Journal, 708, 1254

Aharonian, F., Akhperjanian, A., Beilicke, M., et al. 2004, The Astrophysical Journal, 614, 897

Aharonian, F., Akhperjanian, A. G., Bazer-Bachi, A. R., et al. 2006, Astronomy & Astrophysics, 457, 899

Albert, J., Aliu, E., Anderhub, H., et al. 2008a, The Astrophysical Journal, 674, 1037

—. 2007, Nuclear Instruments and Methods in Physics Research A, 583, 494

—. 2008b, Nuclear Instruments and Methods in Physics Research A, 588, 424

Aleksić, J., Alvarez, E. A., Antonelli, L. A., et al. 2012, Astroparticle Physics, 35, 435

Aleksić, J., Ansoldi, S., Antonelli, L. A., et al. 2014a, ArXiv e-prints, arXiv:1409.6073

—. 2014b, ArXiv e-prints, arXiv:1409.5594

Arons, J., & Tavani, M. 1994, ApJS, 90, 797

Atoyan, A. M. 1999, Astronomy & Astrophysics, 346, L49

Atoyan, A. M., & Aharonian, F. A. 1996, MNRAS, 278, 525

Atwood, W. B., Abdo, A. A., Ackermann, M., et al. 2009, The Astrophysical Journal, 697, 1071

Bednarek, W., & Bartosik, M. 2003, Astronomy & Astrophysics, 405, 689

—. 2005, Journal of Physics G Nuclear Physics, 31, 1465

Bucciantini, N., Arons, J., & Amato, E. 2011, MNRAS, 410, 381

Buehler, R., Scargle, R. D., et al. 2012, The Astrophysical Journal, 749, 26

Bühler, R., & Blandford, R. 2014, Reports on Progress in Physics, 77, 066901

de Jager, O. C., & Harding, A. K. 1992, The Astrophysical Journal, 396, 161

de Jager, O. C., Harding, A. K., Michelson, P. F., et al. 1996, The Astrophysical Journal, 457, 253

Del Zanna, L., Volpi, D., Amato, E., & Bucciantini, N. 2006, Astronomy & Astrophysics, 453, 621

Fomin, V. P., Stepanian, A. A., Lamb, R. C., et al. 1994, Astroparticle Physics, 2, 137

Hester, J. J. 2008, ARA&A, 46, 127

Hillas, A. M., Akerlof, C. W., Biller, S. D., et al. 1998, The Astrophysical Journal, 503, 744

James, F. 1998, MINUIT Reference Manual (CERN Program Library Long Writeup D506)

Kennel, C. F., & Coroniti, F. V. 1984, The Astrophysical Journal, 283, 710

Lombardi, S. 2011, in International Cosmic Ray Conference, Vol. 3, International Cosmic Ray Conference, 262

Martín, J., Torres, D. F., & Rea, N. 2012, MNRAS, 427, 415

Meyer, M., Horns, D., & Zechlin, H. 2010, Astronomy & Astrophysics, 523, A2+

Pétri, J., & Lyubarsky, Y. 2007, Astronomy & Astrophysics, 473, 683

Sironi, L., & Spitkovsky, A. 2011, The Astrophysical Journal, 741, 39

Stephenson, F. R., & Green, D. A. 2003, Astronomy, 31, 118903

Tanaka, S. J., & Takahara, F. 2010, The Astrophysical Journal, 715, 1248

Tavani, M., Bulgarelli, A., Vittorini, V., et al. 2011, Science, 331, 736

Tikhonov, A. N., & Arsenin, V. I. 1979, Methods of Solution of Ill-posed Problems

Torres, D. F., Cillis, A. N., & Martín Rodriguez, J. 2013a, The Astrophysical Journal, Letters, 763, L4

Torres, D. F., Martín, J., de Oña Wilhelmi, E., & Cillis, A. 2013b, MNRAS, 436, 3112

van der Swaluw, E., Achterberg, A., Gallant, Y. A., & Tóth, G. 2001, Astronomy & Astrophysics, 380, 309

Volpi, D., Del Zanna, L., Amato, E., & Bucciantini, N. 2008, Astronomy & Astrophysics, 485, 337

Weekes, T. C., Cawley, M. F., Fegan, D. J., et al. 1989, The Astrophysical Journal, 342, 379

Wilson-Hodge, C. A., Cherry, M. L., Case, G. L., et al. 2011, The Astrophysical Journal, Letters, 727, L40

Zanin, R., et al. 2013, in International Cosmic Ray Conference, International Cosmic Ray Conference